Acta Materialia 243 (2023) 118515

Contents lists available at ScienceDirect

Acta Materialia

journal homepage: www.elsevier.com/locate/actamat

Full length article

Ultra-strong heavy-drawn eutectic high entropy alloy wire

Jin-Xi Chen[a,b,1], Tong Li[a,b,1], Yan Chen[a,b,*], Fu-Hua Cao[a,b], Hai-Ying Wang[a,b], Lan-Hong Dai[a,b,c,*]

[a] State Key Laboratory of Nonlinear Mechanics, Institute of Mechanics, Chinese Academy of Sciences, Beijing 100190, PR China
[b] School of Engineering Science, University of Chinese Academy of Sciences, Beijing 101408, PR China
[c] School of Future Technology, University of Chinese Academy of Sciences, Beijing 100049, PR China

ARTICLE INFO

Article history:
Received 9 August 2022
Revised 7 November 2022
Accepted 11 November 2022
Available online 12 November 2022

Keywords:
Eutectic high entropy alloy wire
Mechanical properties
Gradient heterogeneous lamella structure
Cross-slip

ABSTRACT

Metallic wires with high strength-ductility at both room and cryogenic temperatures are always pursued for engineering applications. However, traditional metallic wires are tortured inevitably by strength-ductility trade-off dilemma. In this work, a gradient heterogeneous lamella structure, characterized with hard gradient-distributed B2 lamellae embedded in soft FCC lamellae matrix, is introduced into $AlCoCrFeNi_{2.1}$ eutectic high entropy alloy (EHEA) wire by well-designed multiple-stage heavy-drawn and heat treatment processes, which achieves an outstanding strength-ductility synergy. This EHEA wire exhibits not only high tensile strength of 1.85 GPa and sufficient uniform elongation of ~12% at room temperature, but also ultra-high tensile strength of 2.52 GPa and even slightly elevated uniform elongation of ~14% at cryogenic temperature. In-depth microstructure characterization indicates that the gradient heterogeneous lamella structure facilitates a radial gradient distribution of geometrically necessary dislocation (GND) during tension, i.e., the GND density decreases gradually from the surface region to the central region of EHEA wire, which induces pronounced strain gradient strengthening effect and thus greatly benefits the mechanical properties. Intriguingly, at cryogenic temperature, dense cross-slip which gives rise to intensively dynamic microstructure refinement is firstly observed in the B2 phase of EHEA wire. The activation of cross-slip provides sufficient ductility while inducing evidently dynamic Hall-Petch effect, becoming the most effective deformation mechanism contributing to the unprecedented cryogenic tension properties. This work sheds light on designing ultra-strong EHEA wire and other advanced metallic wires.

1. Introduction

Metallic wires with high strength and ductility are highly desired for various engineering applications, such as large cable-stayed bridge, heavy lift slings, offshore platform rigging and so on, among which pearlitic steel wires stand out to be the most mature and widely used materials [1–3]. However, high strength is usually accompanied with low ductility, known as trade-off dilemma [4]. Besides, the environments in which metallic wires served have also become much more complex and extreme, e.g., cryogenic environments, which poses a great challenge to conventional metallic wires. Hence, developing high performance metallic wires that can safely serve under various harsh circumstances is urgently required.

During past decade, high entropy alloys (HEAs) or complex concentrated alloys (CCAs), i.e., the material systems with multiple principal elements in equi-molar or near-equimolar ratio, have attracted a constant upsurge [5–17]. The unique design concept endows these alloys with a variety of unexpected mechanical properties [18–29], such as excellent fracture toughness at cryogenic temperature [30] and extraordinary self-sharpening ability [31], which making them novel and potential candidates for engineering application. Recently, Lu et al. [32,33] proposed a design strategy of eutectic high entropy alloys (EHEAs) and produced an $AlCoCrFeNi_{2.1}$ EHEA with regular FCC/B2 lamellar structures, which could accomplish more excellent combination of strength and ductility at both room and cryogenic temperatures [34]. Then, significant efforts have been devoted to optimizing the mechanical properties of $AlCoCrFeNi_{2.1}$ EHEAs [35–41]. For example, Shi et al [37] developed a two-hierarchical heterogeneous structure in EHEAs and thus achieved a superior strength-ductility combination, Reddy

* Corresponding authors at: State Key Laboratory of Nonlinear Mechanics, Institute of Mechanics, Chinese Academy of Sciences (CAS), Beijing 100190, China.
E-mail addresses: chenyan@lnm.imech.ac.cn (Y. Chen), lhdai@lnm.imech.ac.cn (L.-H. Dai).
[1] These authors contribute equally to this work.

https://doi.org/10.1016/j.actamat.2022.118515
1359-6454/

et al [38] developed a unique dual structure-compositional heterogeneities EHEA and thereby achieved almost the best strength in EHEAs, Ren et al [41] recently used laser powder bed fusion to print nanolamellar EHEA and obtained a remarkable strength-ductility combination. Therefore, the appearance of $AlCoCrFeNi_{2.1}$ EHEA provides us with huge possibilities for fabricating advanced metallic wires with ultra-high strength and sufficient ductility under extreme circumstances.

It is noteworthy that, heterogeneous materials, such as materials with gradient structure [19] or heterogeneous lamella structure [37,38,42], usually possess superior mechanical properties. Fortunately, it is reported that the conditions of drawn process (die angle and amount of reduction per pass) can effectively affect strain distribution along the radial direction of wire [43], and the mechanical properties of the drawn wire are correlated with the heterogeneous microstructures, such as grain refinement effect brought about by deformation twinning [44]. Accordingly, in order to achieve unprecedented mechanical properties in EHEA wire for extreme engineering applications, introducing a gradient structure combined with the internal lamellar structures of EHEAs by appropriately adjusting the drawn and subsequent heat treatment processes becomes an attractive strategy.

In this work, multiple-stage heavy-drawn and heat treatment processes are elaborately designed to fabricate EHEA wire. Following this strategy, an $AlCoCrFeNi_{2.1}$ EHEA wire with a gradient heterogeneous lamella structure is successfully fabricated. This EHEA wire with a diameter of 500 μm exhibits not only extraordinary tension properties at room temperature (293 K) but also much better tension properties at cryogenic temperature (77 K). Then, the internal relationships between thermomechanical processing, structural features, deformation mechanisms and mechanical properties are systematically studied by a series of microstructure characterizations, e.g., electron backscattered diffraction (EBSD) and transmission electron microscope (TEM).

2. Method

2.1. Materials

Ingots of $AlCoCrFeNi_{2.1}$ EHEA were prepared from commercially pure metals of 99.9 wt.% purity. The raw materials were alloyed in a BN crucible in the vacuum induction melting furnace. The pouring temperature was set to be 1773 K. Master alloys ingots about 5.0 kg were melted, superheated and poured into a cylindrical MgO crucible with the length of 300 mm and inner diameter of 30 mm. The casting was turned on a lathe to reduce its diameter from 30 mm to 26 mm, cut into a 280-mm-long piece.

The casting rod was hot-rolled to 8.5 mm in steps along the longitudinal direction. Before the first rolling pass, the rod was preheated at 1213 K for 1 h; between all subsequent passes, reheating to 1213 K was done for about 30 min. The 8.5 mm rod was then hot-drawn to 4 mm at 1073 K. The drawing speed was 4 m/min, and the initial holding time of the heat-treatment was 10 min. To remove the oxide coating from the surface, the 4.0 mm wire was then simply polished to 3.5 mm. After that, the 3.5 mm wire was cold-drawn to 500 μm at room temperature, and the drawing speed was also 4 m/min. Besides, after every five passes, the cold-drawn wire was annealed at 1323 K for about 10 min. Finally, the as-drawn wire was annealed at 813 K for about 20 h.

2.2. Tension test

Specimens with a gauge length of 50 mm were tested using a UTM 4204 electromechanical universal testing machine at a strain rate of 1×10^{-3} s^{-1}. Both ends of the specimens were fixed between two pieces of aluminum alloy plates. Uniaxial tension tests were performed at room and liquid-nitrogen temperatures, respectively. In the cryogenic tests, the samples and clamps were fully immersed in liquid nitrogen all the time, and held for 30 min before the tests began. For each temperature, at least three samples were tested.

2.3. Microstructure characterization

Morphologies of the EHEA wires were characterized by scanning electron microscope (SEM, JSM-7900F). The phase thickness, average grain size and aspect ratio were all measured by EBSD using a field emission SEM equipped with EDAX-TSL OIM EBSD system, the step size was 100 nm. The focused ion beam (FIB) instrument (Scios2) was applied to fabricate TEM samples, the TEM foils were all cut from the center of wires. TEM images and corresponding selected area electron diffraction (SAED) patterns, high-resolution TEM (HRTEM) images, energy-dispersive x-ray spectroscopy (EDS) mapping and the high-angle annular dark field (HAADF) images were all conducted on JEM-2100F at 200 kV.

3. Result

3.1. Microstructure evolution during thermomechanical processes

In order to introduce the ideal gradient heterogeneous lamella structure into EHEA wire, we carried out well-designed multiple-stage processes, mainly including hot-rolling, hot-drawing, cold-drawing and subsequent annealing, as described in the section of method. Here, we demonstrate our design thought for the microstructure evolution hidden in the procedure by taking advantage of the schematic diagram, as shown in Fig. 1a, where the FCC and B2 phases are represented in cyan and pink, respectively. Generally, the as-cast $AlCoCrFeNi_{2.1}$ EHEA exhibits a typical lamellar eutectic morphology composed of mutual alignment of the FCC and B2 phases, but the FCC and B2 lamellae within a single colony possess their own similar orientation, while completely differ with those in the neighboring colonies [45]. In order to adjust the orientation of FCC and B2 lamellae into similar direction for better formability and maintain the integrity of lamella structure, hot-rolling and hot-drawing are selected. By using these two processes in turn, the microstructure of EHEA can be well rearranged and refined. Then, in order to introduce a gradient structure based on its lamella structure and strengthen EHEA wire, cold-drawing process should be designed elaborately. Since the B2 lamellae are relatively brittle at room temperature, by increasing the die angle and amount of reduction appropriately, the lamella structure in the surface region will be severely broken, while the lamella structure in the central region will be almost unaffected. Consequently, the gradient heterogeneous lamella structure is introduced into EHEA wire by multiple-stage heavy-drawn processes. Finally, in order to endow the EHEA wire with sufficient ductility and preserve the gradient heterogeneous lamella structure, partial recovery should be promoted while recrystallization should be completely prevented, thereby careful control of annealing is much vital.

To verify the effectiveness of our design, we selected three distinct positions, i.e., surface, middle (about 120 μm away from the surface) and center of as-drawn wire and annealed wire, and performed EBSD analysis. As expected, there is no detectable difference in the phase maps and IPF maps before and after annealing, implying that the recrystallization was completely prevented, where the phase maps and IPF maps of annealed wire are shown in Fig. 1b–g. The overall morphologies of as-drawn wire and annealed wire still maintain the lamellar structure and mutual alignment of two phases, where the FCC and B2 phases are represented

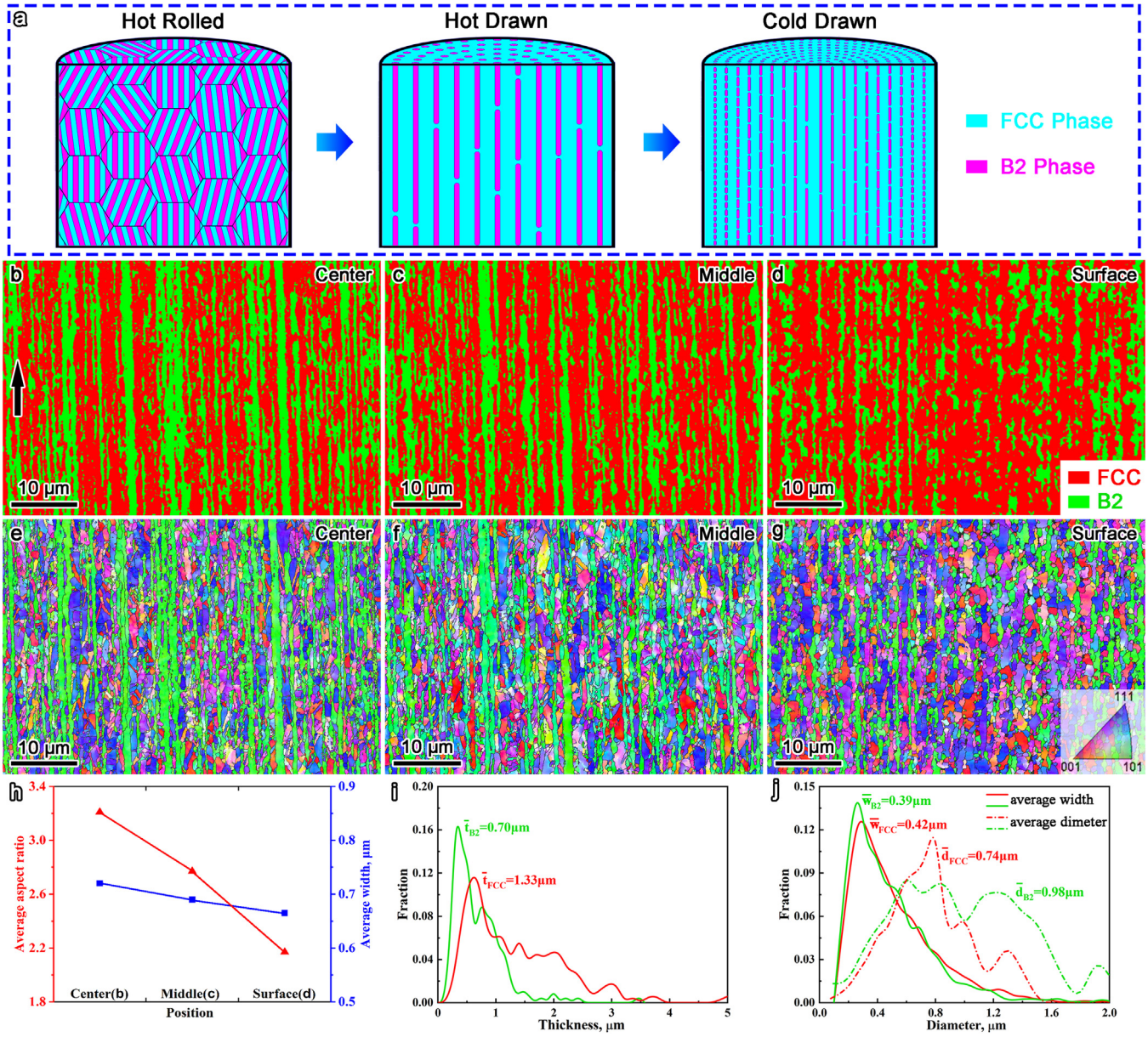

Fig. 1. (a) Schematic diagram shows the design thought of the gradient heterogeneous lamella structure, where the FCC and B2 phases are shown in cyan and pink, respectively. EBSD (b–d) phase maps and (e–g) IPF maps of annealed EHEA wire from the central region to surface region show the gradient heterogeneous lamella structure, where the FCC and B2 phases are shown in red and green, respectively. (h) The distributions of average aspect ratio and average width of B2 phase in EHEA wire from the central region to surface region. (i) The distributions of phase thicknesses in EHEA wire, plotted in terms of the area fraction. (j) The distributions of average widths and average diameters of FCC and B2 grains in EHEA wire, plotted in terms of the area fraction. The FCC and B2 phases are shown in red and green, respectively.

in red and green, respectively. Most importantly, a gradient heterogeneous lamella structure is clearly observed from the central region to the surface region, where the hard gradient-distributed B2 lamellae that embedded in soft FCC lamellae matrix are more continuous in the central region but more discontinuous in the surface region. More specifically, as shown in Fig. 1h, the average aspect ratio of B2 phase decreases significantly from the central region (~3.2) to the surface region (~2.2), but the average width of B2 phase can be regarded as almost unchanged from the central region (~0.72 μm) to the surface region (~0.67 μm), further implying the gradient-distribution of the B2 lamellae. Besides, the grain shapes of two phases, especially the B2 grains, also show similar trends, that the closer to the center, the longer the grains are. Then, the IPF maps (Fig. 1e–g) imply that the preferred orientations of the FCC and B2 phases in EHEA wire along the axial direction (marked by black arrow in Fig. 1b) are $<111>_{FCC}$ and $<101>_{B2}$, respectively. By statistics, the volume fractions of FCC and B2 phases are ~61% and ~39%, the average phase thicknesses of FCC and B2 phases are ~1.33 and ~0.70 μm (Fig. 1i), the average widths of FCC and B2 grains are ~0.42 and ~0.39 μm, the average diameters of FCC and B2 grains are ~0.74 and ~0.98 μm (Fig. 1j), and the aspect ratios of FCC and B2 grains are ~2.80 and ~4.64, respectively.

Fig. 2a further shows the IPFs of FCC and B2 phases in EHEA wire in radial (R), hoop (θ) and axial directions (Z). In both radial and hoop directions, the preferred orientations of FCC and B2 phases are $<101>_{FCC}$ and $<111>_{B2}$, respectively, while in the axial direction, the preferred orientations of FCC and B2 phases change to $<111>_{FCC}$ and $<101>_{B2}$, respectively, which confirms a Kurdjumov–Sachs (K-S) type orientation relationship between

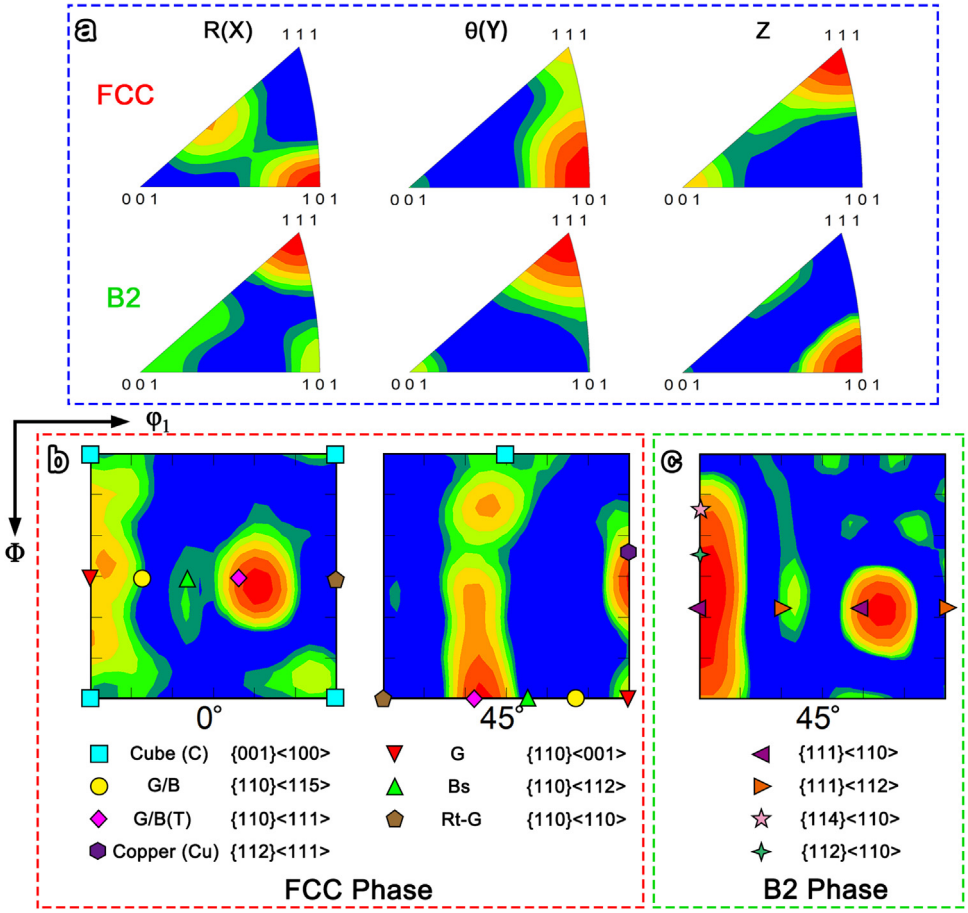

Fig. 2. (a) IPFs of FCC and B2 phases in EHEA wire in radial (R), hoop (θ) and axial (Z) directions. (b, c) Relevant ODF sections obtained from the EBSD analysis of FCC and B2 phases in EHEA wire. The symbols indicate the positions of typical texture components in FCC-based and BCC-based crystal.

FCC and B2 phases, i.e., $\{111\}_{FCC} \parallel \{011\}_{B2}$ and $\langle\bar{1}01\rangle_{FCC} \parallel \langle\bar{1}\bar{1}1\rangle_{B2}$. Then, as shown in Fig. 2b and 2c, the developments of textures in EHEA wire are obtained by the orientation distribution functions (ODFs), where the main deformation texture components listed below are indicated by different symbols and overlaid on ODF sections. Fig. 2b shows the $\varphi_2 = 0^\circ$ and 45° sections of the ODFs of FCC phase. It can be clearly observed that the FCC phase in EHEA wire shows the strongest intensity at the G/B(T) location, followed by Copper (Cu) and G. Fig. 2c shows the $\varphi_2 = 0^\circ$ section of the ODFs of B2 phase, where the B2 phase in EHEA wire develops a predominant {111}<110> component, followed by {112}<110> and {114}<110> components. By comparison with cold-rolled EHEAs [45], current EHEA wire develops a special combination of textures of two phases in EHEAs.

To further reveal the effects of multiple-stage heavy-drawn process and subsequent heat treatment on the microstructure evolution of EHEA wire, TEM analyses were conducted. From here on, unless otherwise noted, the "EHEA wire" appearing later in this article refers to the "annealed EHEA wire". Fig. 3 shows bright-fight TEM (BF-TEM) images and corresponding SAED patterns of as-drawn EHEA wire. As can be seen in Fig. 3a, the as-drawn EHEA wire is composed of ultrafine lamellar structure, among which high density of dislocations and dislocation cells (DCs) are extensively distributed. Additionally, some deformation twins (DTs) can be occasionally seen. Two SAED patterns imply that the as-drawn EHEA wire only contains disordered FCC phase and ordered B2 phase, no $L1_2$ phase or nano-precipitates are detected. Moreover, enlarged BF-TEM image of B2 phase (Fig. 3b) reveals high density of dislocations piling up at grain and phase boundaries. By contrast, enlarged BF-TEM image of FCC phase (Fig. 3c) shows the activation of some nano-DTs besides the accumulation of dislocations.

Then, Fig. 4 shows the microstructures of annealed EHEA wire. Compared with as-drawn EHEA wire (Fig. 3a), although there is an obvious decrease tendency on the dislocation density of annealed EHEA wire (Fig. 4a), the dislocation density is still very high. Two SAED patterns imply that the EHEA wire still consists of only FCC and B2 phases without any $L1_2$ phase or nano-precipitates. All the phenomena mentioned above together indicate that the EHEA wire successfully processes a partial recovery. Moreover, the HRTEM image uncovers semi-coherent phase boundaries between FCC and B2 phases (Fig. 4b), indicating that the combination of two phases in EHEA wire is at the atomic level and strong enough to bear high stress [46]. The fast Fourier transformation (FFT) further confirms the K-S type orientation relationship between FCC and B2 phases. The semi-coherent phase boundaries and K-S type orientation relationship in EHEA wire are consistent with previous research on bulk $AlCoCrFeNi_{2.1}$ EHEAs [46,47]. By comparison with as-drawn wire, the difference between the microstructures of as-drawn wire and annealed wire is confirmed to be only dislocation density.

Then, Fig. 5 shows enlarged bright-field imaging STEM image at local position in Fig. 4a and corresponding EDS elemental mapping images for Al, Co, Cr, Fe and Ni. Obviously, the EDS mapping images reveal that the FCC phase in EHEA wire is enriched in Co, Cr and Fe, while the B2 phase is enriched in Al and Ni. Table 1 gives a more accurately summary of the average chemical compositions by EDS in TEM. It can be clearly seen that the FCC phase is only depleted in Al, while the B2 phase is depleted in Co, Cr and Fe.

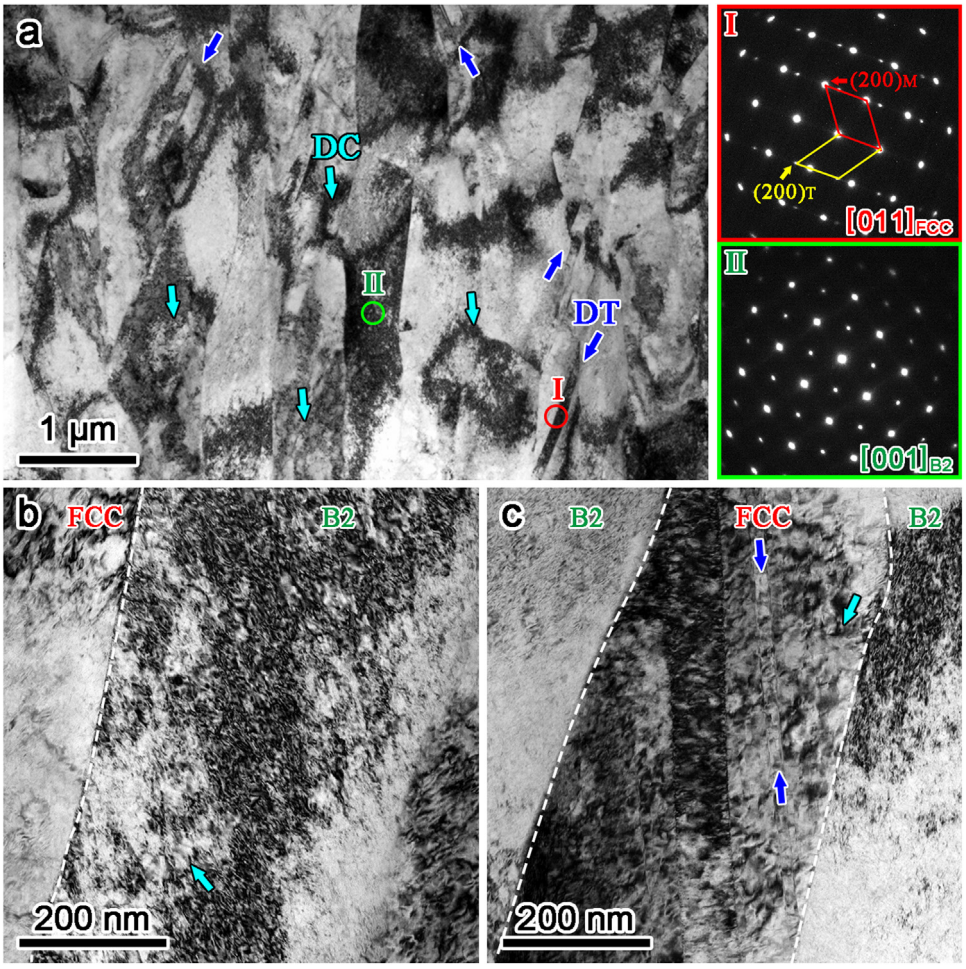

Fig. 3. (a) BF-TEM image of as-drawn EHEA wire, two corresponding SAED patterns are taken along [011] and [001] zone axis, respectively. Enlarged BF-TEM images of (b) B2 phase and (c) FCC phase. The dislocation cells are marked by cyan arrows, the deformation twins are marked by blue arrows.

Table 1
Chemical composition (in at.%) of the EHEA wires analyzed by EDS in TEM.

Phase	Elements				
	Al	Co	Cr	Fe	Ni
Nominal	16.39	16.39	16.39	16.39	34.43
FCC	4.88±0.09	21.52±0.37	24.55±0.43	22.40±0.40	26.65±0.49
B2	29.23±0.47	9.19±0.19	9.93±0.17	8.17±0.16	43.48±0.83

3.2. Tension properties

Fig. 6a shows the tensile engineering stress-strain curves of as-drawn EHEA wire tested at 293 K and annealed EHEA wires tested at 293 K and 77 K. Obviously, after multiple-stage heavy-drawn processes, the as-drawn EHEA wire shows higher yield strength (YS) of ~1.75 GPa and ultimate tensile strength (UTS) of ~1.94 GPa, but its total tensile elongation is much limited (~2.3%). However, after annealing at a moderate temperature, the EHEA wire successfully exhibits excellent strength-ductility balance at 293 K, whose YS, UTS and uniform elongation are about 1.57 GPa, 1.85 GPa and 12.1%. Intriguingly, it is found that the EHEA wire could even achieve ultra-high strength by decreasing temperature from 293 K to 77 K, whose YS and UTS are increased to 2.25 and 2.52 GPa, respectively, meanwhile the uniform elongation could also be slightly improved to 14.3%. Then, the tensile true stress-strain curves and hardening rate curves of EHEA wires are calculated, as shown in Fig. 6b. Evidently, the work-hardening capability of EHEA wires is much more pronounced and stable at 77 K, but exhibits a relatively continuous decrease tendency at 293 K. To the best of our knowledge, the strength-ductility combination achieved at 293 K is ahead of most previously reported EHEAs [33–41,46,48–54], as shown in Fig. 6c. Furthermore, the strength-ductility combination achieved at 77 K are extremely difficult to achieve for traditional metallic wires [55–58] and even major bulk metals [34,57–83], as shown in Fig. 6d, which successfully exhibits a giant potential for structural applications under various harsh circumstances.

3.3. Deformation mechanisms

In order to uncover the underlying mechanisms at 293 K and 77 K, the microstructures of EHEA wires that conducted uniaxial tension tests were further characterized in detail. Fig. 7a shows the BF-TEM images of fractured EHEA wire tested at 293 K. Massive dislocations tangle and form abundant dislocation cells in both FCC and B2 phases, deviding grains into smaller sub-grains. Enlarged BF-TEM image of B2 phase demonstrates the motion of dislocations without any other special features (Fig. 7b). By contrast, as shown

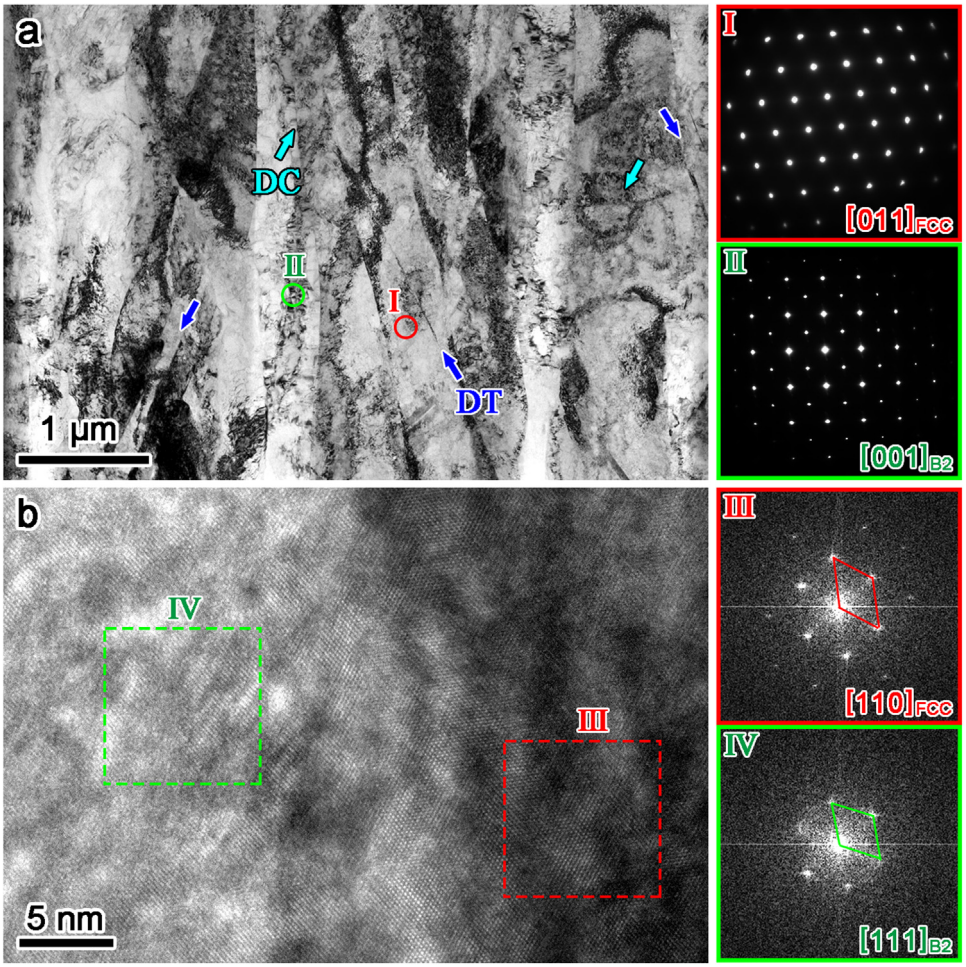

Fig. 4. (a) BF-TEM image of annealed EHEA wire, two corresponding SAED patterns are taken along [011] and [001] zone axis, respectively. (b) HRTEM image shows the semi-coherent phase boundaries between FCC and B2 phases.

in Fig. 7c and 7d, enlarged BF-TEM images of FCC phase demonstrate plenty of fine and short stacking faults (SFs) extending in the same direction, some of which have already evolved into nano-DT lamellar. Therefore, it can be determined that the B2 phase in EHEA wire exhibits dislocation-induced plasticity, while the FCC phase exhibits both dislocation-induced plasticity and SF-induced plasticity at 293 K.

Then, two samples conducted different levels of accumulated strain at 77 K were investigated to obtain a better comprehension on the unprecedented cryogenic tension properties of EHEA wire. As shown in Fig. 8a, at an engineering strain of 5%, several wavy slip patterns in B2 phase are clearly observed, indicating that the cross-slip is already activated at this stage. Then, at an engineering strain of 14.3% (i.e., fracture strain), not only abundant deformation twins and dislocation cells are still widely distributed in FCC phase, but also extensive slip traces of the {112} slip planes are visible in many B2 grains (Fig. 8b, c). Therefore, at 77 K, the {112} <111> becomes one of the main slip systems in B2 structure, which has been observed in NiAl-type B2 structure and several BCC structure by many reported studies [84,85]. According to double-beam BF-TEM image (Fig. 8d), it can be clearly observed that the activation of cross-slip results in strong interaction of slip traces in B2 phase, as reported in recent work about FeCoNiCrMn [86]. It is noted that previous research revealed the cross-slip being occasionally activated in the FCC phase [18,46,47], but never in the B2 phase of EHEAs. Here, it is the first time to demonstrate the activation of cross-slip in the B2 phase of EHEAs, which results in strong grain refinement during deformation. By contrast, HRTEM image and corresponding FFT detect quantities of stacking faults extending along multiple {111} planes in FCC grains (Fig. 8e, f), some of which have also evolved into nano-DTs. The stacking faults and nano-DTs have strong interactions with each other and gradually form unusual 3D SF-DT structure networks, also inducing efficiently dynamic microstructure refinement and becoming the main deformation mechanism in FCC phase, as reported in gradient cell-structured HEAs [19].

3.4. Fracture morphologies

As shown in Fig. 9a, the fracture surface of as-drawn EHEA wire consists of a less rugged central region and a more rugged lateral region at 293 K. At high magnification (Fig. 9b), numerous small dimples could be observed at central region, indicating its ductile fracture. Then, the fractured EHEA wire tested at 293 K shows a relatively flat fracture surface at low magnification (Fig. 9c) but still a clearly ductile fracture surface consisting of massive dimples at high magnification (Fig. 9d). When the temperature drops from 293 K to 77 K, the fractured EHEA wire exhibits a clearly cup-and-cone fracture surface (Fig. 9e). Besides, at high magnification (Fig. 9f), it is clearly observed that the depth of the dimple increases, which further implies the better ductility at 77 K.

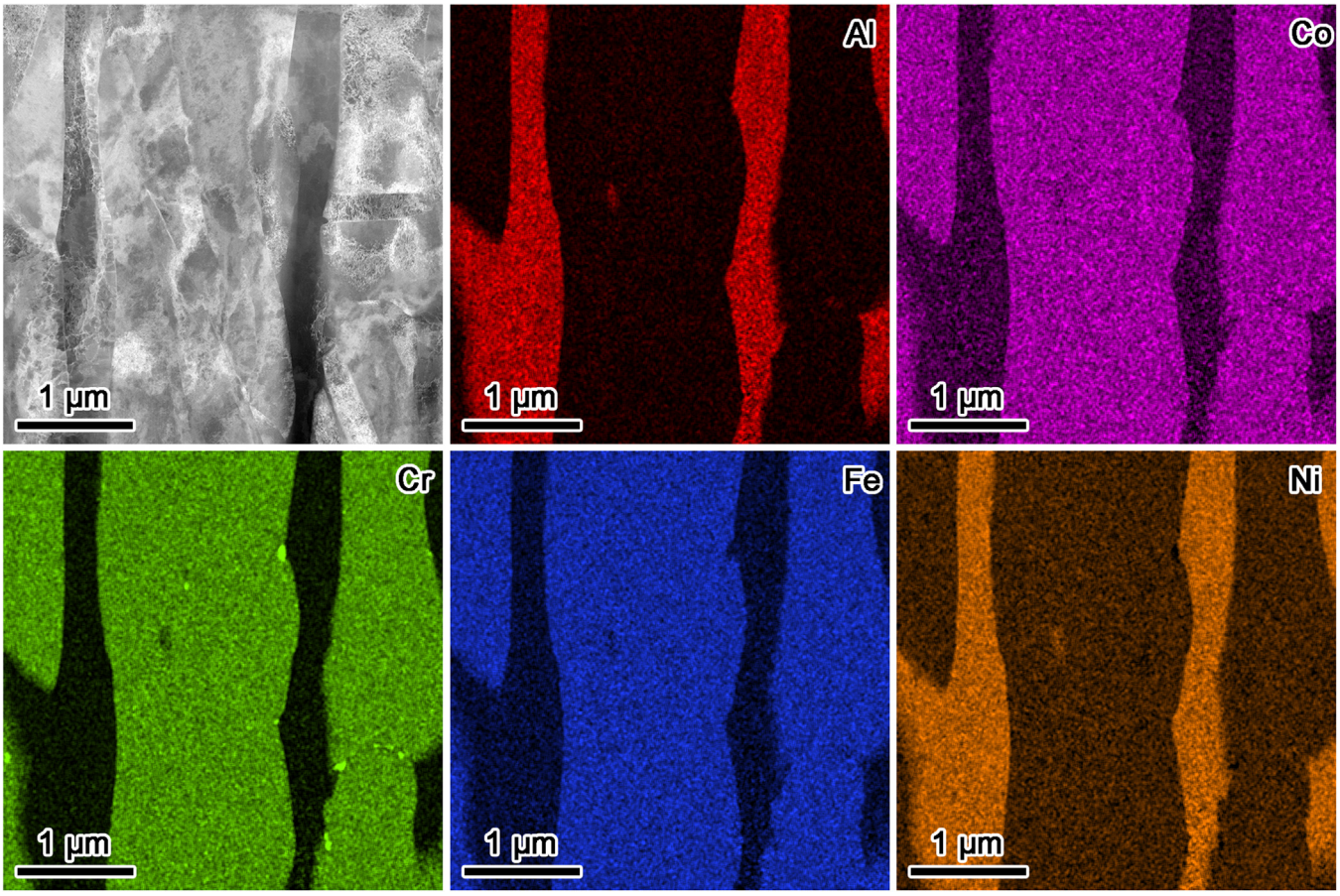

Fig. 5. Elemental mapping results show that the FCC phase in EHEA wire is enriched in Co, Cr and Fe, while the B2 phase is enriched in Al and Ni.

4. Discussion

4.1. Tension properties at 293 K

By carefully selecting materials and elaborately carrying out multiple thermomechanical processes, numerous structural features introduced, i.e., the gradient heterogeneous lamella structure, special combination of textures, semi-coherent phase boundaries and the K-S type orientation relationship, endow EHEA wire with quantities of advantages for better mechanical properties.

First, the inherited lamella structure greatly favors the synergies of strength and ductility, where the FCC matrix mainly undergoes severe plastic deformation while the long B2 lamellae play a vital role in strengthening materials by hindering the dislocation motion, which is a typical superiority of lamellar EHEAs [35–41]. Then, the gradient distribution of B2 lamellae further benefits the combination of strength and ductility. In the surface region, since the B2 phase is more discontinuous, the restriction to the FCC lamellae on both sides is greatly relaxed, so that the plastic deformation of FCC lamellae could be effectively coordinated through the gap between two discontinuous B2 lamellae upon application of strain. Accordingly, it is speculated that the surface region acts as “soft” domain mainly coordinating non-uniform plastic deformation while the central region acts as “hard” domain mainly strengthening materials.

In addition, previous research on FCC alloys revealed that the FCC single crystals loaded along the <111> direction presented the highest strength while those tested along <110> showed the lowest strength [87]. Therefore, it is speculated that the FCC phase in current EHEA wire could exhibit its strength as much as possible due to its predominant textures along the “hardest” <111> direction, which is consistent with typical cold-drawn FCC-based wires, such as Cu-Ag composite [88]. On the one hand, the change of preferred textures in FCC phase is thought to be beneficial to the whole strength of EHEA wire. On the other hand, the relevant decrease of hardness difference between two phases also reduces the probability of early cracking in local domains and thus facilitates the whole ductility of EHEA wire.

Besides, given that current EHEA wire has semi-coherent phase boundaries, which are strong enough to accommodate high stress due to their chemically disordered features [47] and thus could be regarded as barriers and sinks for dislocations, the K-S type orientation relationship could further offer strong interfacial bonding and numerous possibilities for slip transfer between two phases, and thus have great contributions to both strength and ductility [40]. Moreover, current EHEA wire is composed of two types of columnar grains with ultrafine widths, which could induce intensive grain boundary hardening and thus result in high strength, known as Hall-Petch relation [89]. Finally, it is reported that no obvious dislocations were observed in the B2 phase of as-cast EHEA [75]. However, according to systematical characterizations above, massive dislocations detected in B2 grains imply that the B2 phase in current EHEA wire can plastically deform and sustain hardening in tension, which could significantly reduce the possibility of early failure, even with ultra-high strength.

Kernel Average misorientation (KAM) is an OIM analysis tool that characterizes the local misorientation [90], which can clearly visualize the intragranular rotations during deformation. In order to further investigate the effect of structural features on deformation behavior, half the cross-sectional areas of EHEA wire

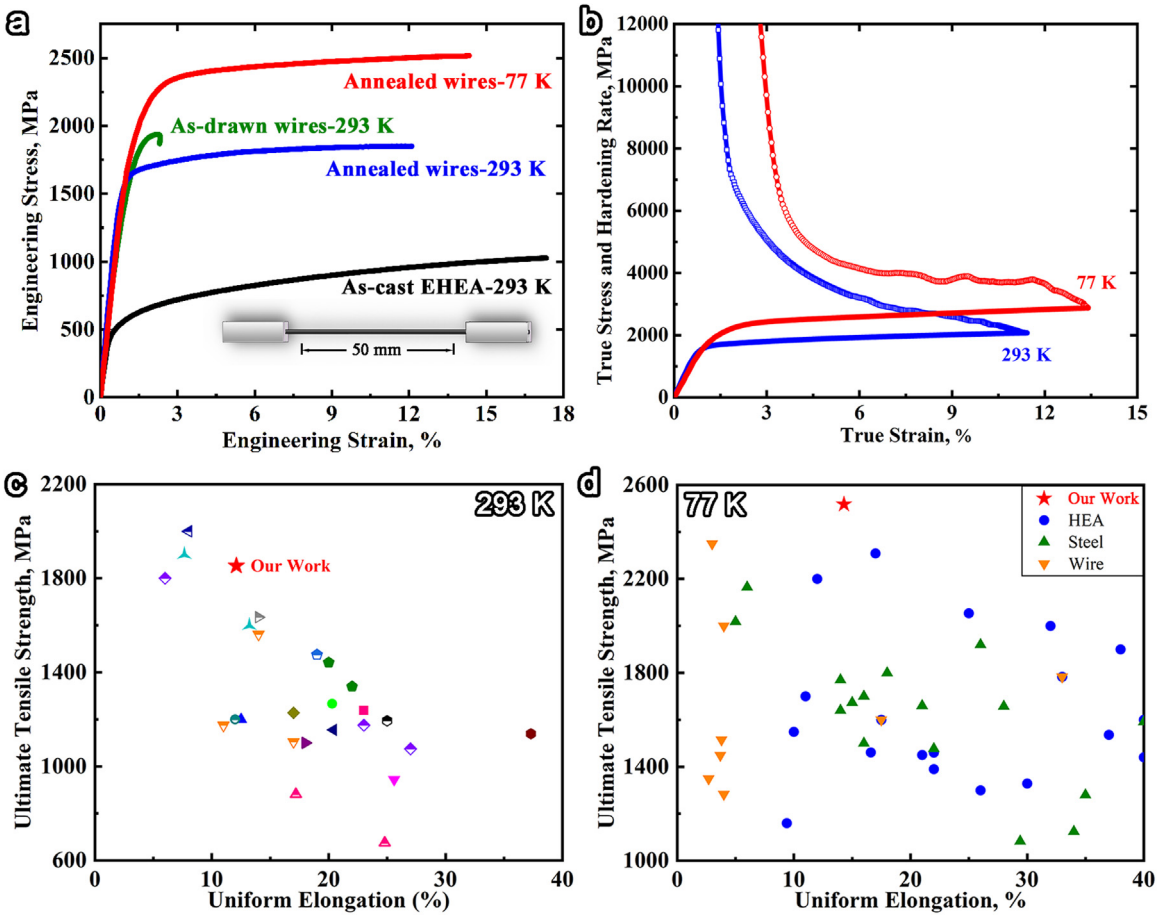

Fig. 6. (a) Tensile engineering stress-strain curves of as-drawn EHEA wire, annealed EHEA wires and as-cast EHEA. (b) True stress-strain curves and hardening rate-true strain curves of EHEA wires at 293 K and 77 K. (c) Maps of ultimate tensile strength vs. uniform elongation of current EHEA wire and bulk EHEAs [33–41,46,48–54] at 293 K. (d) Maps of ultimate tensile strength vs. uniform elongation of current EHEA wire, metallic wires [55–58] and bulk metals [34,57–83] at 77 K.

before and after tension were characterized by EBSD KAM maps. As shown in Fig. 10b, before tension, the overall distribution of local misorientation angles is relatively homogeneous, indicating a relatively uniform deformation state of EHEA wire. Combined with previous phase maps (Fig. 1b–d), current KAM map (Fig. 10b) suggests that the uneven strain distribution and corresponding dislocations introduced during multiple-stage heavy-drawing process are almost eliminated through effective recovery while the gradient heterogeneous lamella structure is well preserved.

After tension at 293 K, the distribution of local misorientation angles changes dramatically. As shown in Fig. 10c, a distinct gradient on the distribution of local misorientation angles is detected from surface to center. The closer it is to the surface of EHEA wire, the greater the average misorientation angles are, indicating the surface region experienced much more severe plastic deformation during tension. Geometrically necessary dislocation (GND) represents an extra storage of dislocations required to accommodate the lattice curvature that arises whenever there is a non-uniform plastic deformation [91,92]. In order to quantify the heterogeneity of plastic deformation, the GND densities of two phases before and after tension at 293 K are calculated. The average GND density can be estimated from KAM by the equation [93]: $\rho_{GND} = \frac{\alpha\theta_{KAM}}{Xb}$, where α is a parameter that depends on the grain boundary type and is equal to 2 for tilt boundaries, θ_{KAM} is the average misorientation, $X = np$ is the kernel size, n is the defined nearest neighbor and is equal to 1 here, p is the scan step and is equal to 0.1 μm, b is the Burgers vector (0.254 nm for the FCC matrix, 0.498 nm for B2 lamellae [39]).

Consequently, the distributions of GND densities are shown in Fig. 10d. It is confirmed that the GND densities of both FCC and B2 phases in EHEA wire before loading are truly high but relatively uniform, which are 1.8×10^{15} and 0.8×10^{15} m^{-2}, respectively. The high yield strength of current EHEA wire is enabled by the gradient heterogeneous lamella structure and further enhanced by the high density of dislocations preserved after partial recovery. After tension at 293 K, it is noted that the GND densities of both FCC and B2 phases display gradient distributions, that the closer to the surface, the higher the GND densities are. More specifically, the GND density of FCC phase decreases from 2.6×10^{15} m^{-2} in the surface region to 1.8×10^{15} m^{-2} in the central region, the GND density of B2 phase decreases from 2.0×10^{15} m^{-2} in the surface region to 1.0×10^{15} m^{-2} in the central region, the average GND densities of FCC and B2 phases are approximately 2.3×10^{15} and 1.7×10^{15} m^{-2}, respectively. Since the B2 phase is still much harder than FCC phase, the GNDs required to accommodate non-uniform plastic deformation could easily accumulate near phase boundaries. Our results also agree with this, because the local misorientation angles that are greater than 5° (marked by red) are all found to distribute near phase boundaries (Fig. 10c).

To further comprehend the effect of gradient-distributed B2 lamellae on the deformation behavior of EHEA wire, a shear-lag model commonly used in fiber-reinforced composite is quoted, in which the B2 lamellae are regarded as reinforcing fibers. As shear-lag model suggested, the fiber-reinforced composites derive their strength and stiffness wholly or mainly from thin fibers capable of transmitting high loads along their length through the cylindri-

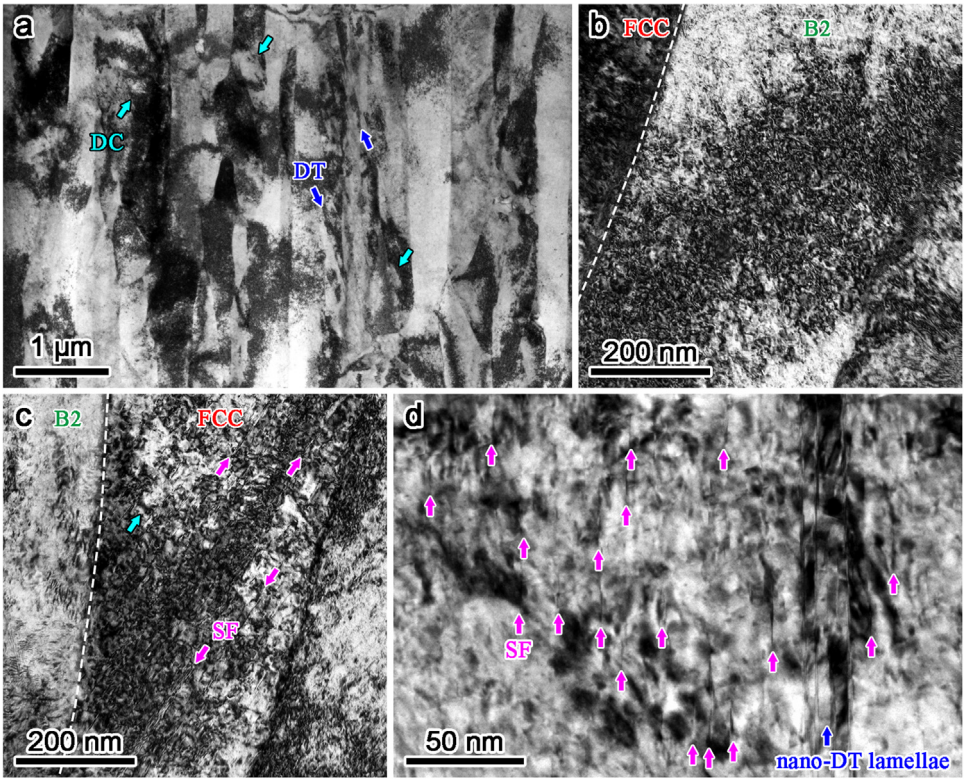

Fig. 7. (a) BF-TEM image of fractured EHEA wire tested at 293 K. Enlarged BF-TEM images of (b) B2 phase and (c, d) FCC phase. The stacking faults are marked by pink arrows.

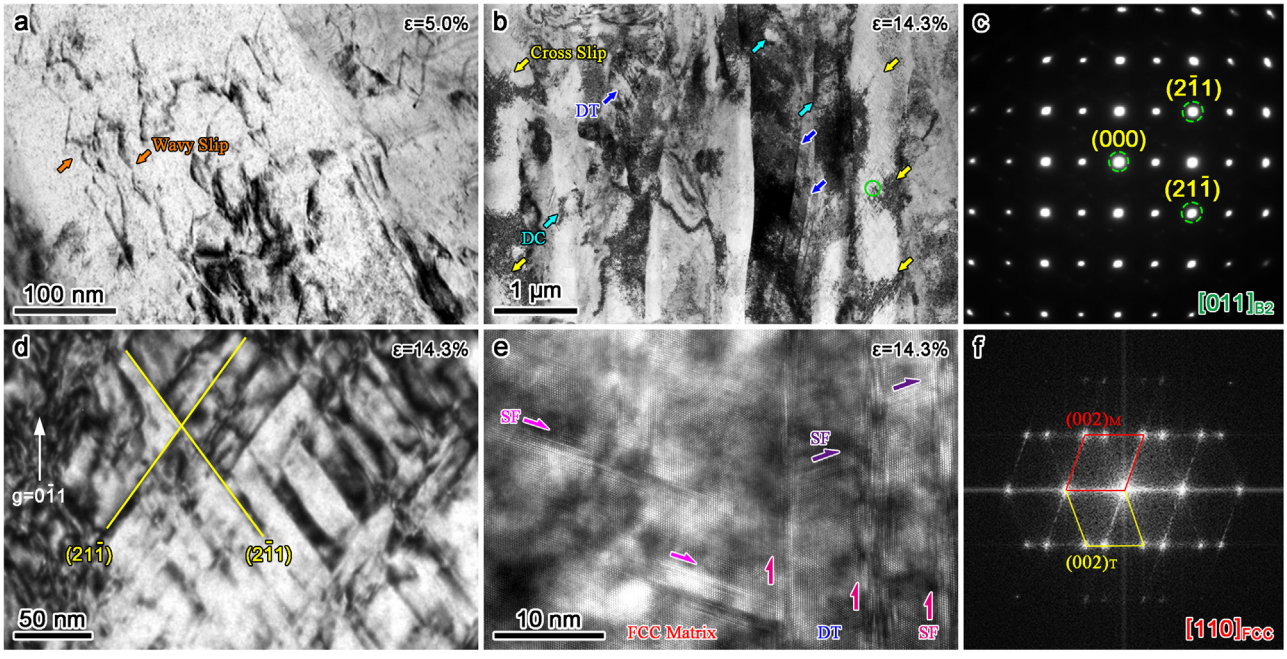

Fig. 8. The evolution of microstructures of EHEA wire with increasing tensile strain at 77 K. (a) BF-TEM image shows wavy slip pattern in B2 phase at an engineering strain of 5.0%. (b) BF-TEM image of fractured EHEA wire (at an engineering strain of 14.3%), and (c) corresponding SAED pattern of cross-slip in B2 phase, taken along [011] zone axis. (d) Double-beam BF-TEM image shows dense cross-slip in B2 phase, where the white arrow with the *g* vector marks the double-beam diffraction condition utilized. (e) HRTEM image and (f) FFT of 3D SF-DT structure networks in FCC phase at an engineering strain of 14.3%. The wavy slip is marked by orange arrows, the cross-slip is marked by yellow arrows, the stacking faults are marked by a series of pink arrows.

cal surface of the fiber [94]. Due to the elastic modulus mismatch between matrix and fiber, the crystal distortion and corresponding shear stress reach the peak at the fiber end. However, it is generally accepted that the distribution of shear stress and crystal distortion is fairly sensitive only within a certain zone near fiber end [95], called "fiber end affected zone" here. In the surface region of current EHEA wire, given that the "B2 fibers" are more discontinuous (or have a much smaller aspect ratio), a higher density of "fiber ends" results in a higher volume fraction of "fiber end affected zone" with severe crystal distortion, which could induce higher GND density during tension. Therefore, the observed gradient distribution of GNDs is thought to be tightly attributed to

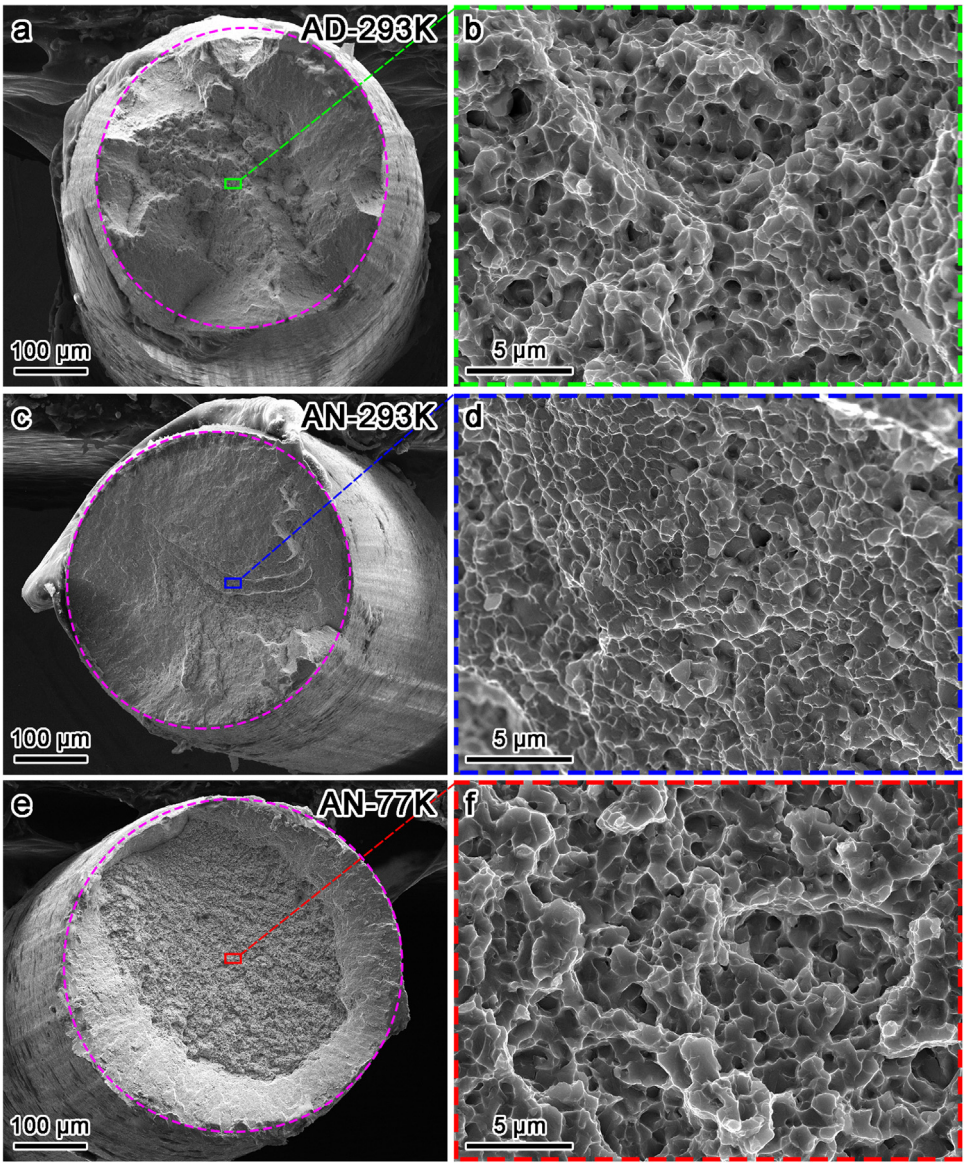

Fig. 9. SEM images of fracture surfaces of (a, b) as-drawn EHEA wire tested at 293 K, (c, d) annealed EHEA wire tested at 293 K and (e, f) annealed EHEA wire tested at 77 K.

the gradient-distributed B2 lamellae. Besides, according to shear-lag model, the fiber axial stress is influenced significantly by the fiber aspect ratio, that the fiber with larger fiber aspect ratio would subject higher the fiber axial stress and thus has greater stress transfer efficiency [95]. Thus, it is again speculated that the central region of EHEA wire acts as "hard" domain while the surface region acts as "soft" domain at the early stage of plastic deformation.

Generally, too much GNDs could lead to higher stress concentration and early nucleation of cracks when lacking ability to coordinate non-uniform plastic deformation, and thus limit the overall ductility of EHEAs. In current EHEA wire, the high GND density near phase boundaries in turn proves the effectiveness of numerous structure features. Furthermore, according to strain gradient theory [96–98], the strain gradient associated with the GNDs is able to cause efficient strengthening effect, which induces high work-hardening capability and homogeneous plastic flow ability. Therefore, during plastic deformation, not only the "hard" domain could greatly strengthen the EHEA wire all the time, but also the "soft" domain could gradually strengthen the EHEA wire through pronounced strain gradient strengthening effect when coordinating non-uniform plastic deformation. Hence, numerous structural features, especially the gradient heterogeneous lamella structure, play the most significant roles in the extraordinary tension properties of EHEA wire at 293 K.

4.2. Tension properties at 77 K

At 77 K, besides the numerous structural features still greatly contributing to the cryogenic tension properties of EHEA wire, multiple deformation mechanisms activated in two phases further enhance the strength-ductility synergy.

Generally, the dislocation motion can be patterned with two prevalent types of mesoscopic deformation modes, planar slip and wavy slip [99]. It is known to all that continuous planar propagation of dislocations often prevails in FCC metals, whereas plasticity in BCC metals is strongly influenced by frequent cross-slip owing to the similarly close-packed {110} and {112} slip planes, resulting in wavy slip patterns [20]. As indicated by TEM analyses (Fig. 8), the cross-slip events in current EHEA wire occurred at an early stage of plastic deformation and developed quickly with the

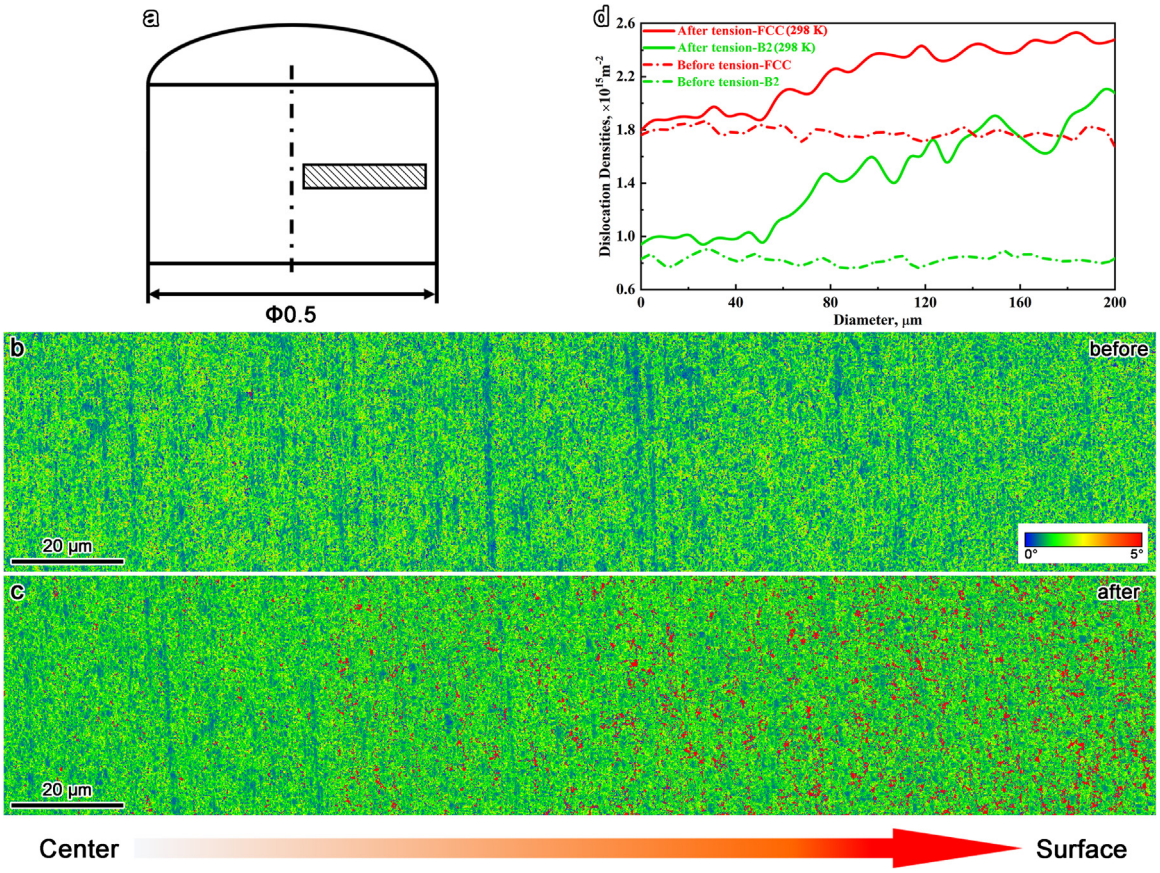

Fig. 10. (a) Schematic representations of the specimens for the EBSD analyses. The KAM maps of EHEA wires (b) before tension and (c) after tension at 293 K. (d) The distributions of GND densities of two phases in EHEA wires before and after tension at 293 K.

increase of plastic deformation. It is reported that the operation of <111> {112} and <111> {110} slip systems in B2 phase could occur at a very high stress [85], thereby the ultra-high operating stresses during plastic deformation of EHEA wire at 77 K are thought to be responsible for the activation of cross-slip.

Additionally, as for $AlCoCrFeNi_{2.1}$ EHEAs, lacking sufficient slip systems in B2 phase is one of the most tortured problems limiting their ductility [46]. Fortunately, the extensive activation of cross-slip in the B2 phase of current EHEA wire could effectively alleviate this problem and thus greatly contribute to the unprecedented cryogenic tension properties of EHEA wire. First, the earlier activation of cross-slip could avoid local stress concentration peak during the early stage of plastic deformation so that inhibit the instability of plasticity. Then, the extensive cross-slip activities could facilitate the strong interactions among dislocations in the primary and secondary slip systems, which may lead to activation of a new slip system [100]. Besides, the high frequency and density of cross-slip events resulted in homogeneously distributed cross-slip networks inside the B2 grains of EHEA wire. The cross-slip networks divided B2 grains into more ultrafine sub-grains, which could induce pronounced high strain hardening by strong dynamic Hall-Petch effect [101] and thus facilitate the plastic flow stability. Finally, double cross-slip could further promote high multiplication rates of dislocations and formation of new Frank-Read sources, thereby facilitate more uniform work-hardening capability [20].

As for FCC phase, it is noted that much more stacking faults are extensively activated and developed at 77 K, which is thought to be relevant to the lowering of SFE on cooling [16]. The extensive activations of stacking faults along multiple {111} planes resulted in unusual 3D SF-DT structure networks (Fig. 7d), which becomes another significant source of high work-hardening capability. First, the 3D SF-DT structure networks can also divide FCC grains into more sub-grains so that induce strong dynamic Hall-Petch effect [102]. Then, due to the strong interaction between dislocations and stacking faults, the additional stress required could hinder the motion of dislocations and thus give rises to the work-hardening capability [103]. Finally, the interaction between two partials probably leads to the formation of Lomer-Cottrell (L-C) locks, which have not only a good ability to accumulate different types of dislocations but also a good stability to resist dissociation [104], when the distance between locks is small, high strengthening could be induced. Therefore, the extensive activations of cross-slip in B2 phase and 3D SF-DT structure networks in FCC phase are two of the most significant sources that allow the EHEA wire to maintain sufficient uniform elongation even with ultra-high strength, for which the unique structural features also provide sufficient preconditions and possibilities.

5. Conclusion

In present study, multiple-stage heavy-drawing and heat treatment processes are carefully designed and harnessed to fabricate EHEA wire. For the first time, a gradient heterogeneous lamellar EHEA wire with ultra-high strength is successfully fabricated. The relationships between structural features, tension properties and deformation mechanisms are detailed investigated and discussed. The following conclusions can be drawn.

1 The gradient heterogeneous lamella structure is characterized with hard gradient-distributed B2 lamellae embedded in soft FCC lamellae matrix, the closer to the surface, the more discontinuous the B2 lamellae are. Then, both FCC and B2 lamellae are composed of columnar grains with ultrafine widths, which

could induce intensive grain boundary hardening. Besides, numerous structural features, e.g., the K-S type orientation relationship, semi-coherent phase boundaries and special combination of textures, could offer strong interfacial bonding and thus contribute to the mechanical properties.

2 With numerous structural features, the EHEA wire exhibits extraordinary tension properties at 293 K, with YS of ~1.57 GPa, UTS of ~1.85 GPa and uniform elongation of ~12.1%. Most importantly, the EHEA wire could even achieve unprecedented tension properties at 77 K, with YS of ~2.25 GPa, UTS of ~2.52 GPa and uniform elongation of ~14.3%.

3 During plastic deformation, the gradient heterogeneous lamella structure causes evident gradient-distributed GND densities in both FCC and B2 phases, i.e., the GND densities decrease gradually from the "soft" surface region to the "hard" central region of EHEA wire, which could induce pronounced strain gradient strengthening effect and thus postpone the necking instability during tension.

4 At 293 K, the B2 phase in EHEA wire exhibits dislocation-induced plasticity, while the FCC phase exhibits both dislocation-induced plasticity and SF-induced plasticity. At 77 K, dense cross-slip is firstly observed in the B2 phase of EHEAs along {112} slip planes, while the stacking faults are extensively activated in the FCC phase along multiple {111} planes and form unusual 3D SF-DT structure networks. The multiple mechanisms in B2 and FCC phases are the most vital factors for the unprecedented cryogenic properties of EHEA wire.

Our investigations not only shed light on the structural features and deformation mechanisms underlying the excellent performance of EHEA wire, but also open up an innovative route for developing new advanced metallic wires that can safely serve under various extreme circumstances.

Declaration of Competing Interest

We confirm that there is no conflict of interest that could have appeared to affect the work reported in this paper.

Acknowledgments

This work is supported by the NSFC (Nos. 11790292, 11972346, 12102433 and No. U2141204), the National Key Research and Development Program of China (No. 2017YFB0702003), the NSFC Basic Science Center Program for "Multi-scale Problems in Nonlinear Mechanics" (No. 11988102), the Strategic Priority Research Program (No. XDB22040302 and No. XDB22040303), the Key Research Program of Frontier Sciences (Grant No. QYZDJSSW- JSC011), Science Challenge Project (No. TZ2016001), the Key Research Program of the Chinese Academy of Sciences (Grant No. ZDRW-CN-2021-2-3), and the opening project of State Key Laboratory of Explosion Science and Technology (Grant No. KFJJ21-01Z).

References

[1] C. Borchers, R. Kirchheim, Cold-drawn pearlitic steel wires, Prog. Mater. Sci. 82 (2016) 405–444, doi:10.1016/j.pmatsci.2016.06.001.
[2] X. Zhang, A. Godfrey, X. Huang, N. Hansen, Q. Liu, Microstructure and strengthening mechanisms in cold-drawn pearlitic steel wire, Acta Mater 59 (2011) 3422–3430, doi:10.1016/j.actamat.2011.02.017.
[3] X. Zhang, N. Hansen, A. Godfrey, X. Huang, Dislocation-based plasticity and strengthening mechanisms in sub-20 nm lamellar structures in pearlitic steel wire, Acta Mater. 114 (2016) 176–183, doi:10.1016/j.actamat.2016.04.040.
[4] Y. Li, D. Raabe, M. Herbig, P.P. Choi, S. Goto, A. Kostka, H. Yarita, C. Borchers, R. Kirchheim, Segregation stabilizes nanocrystalline bulk steel with near theoretical strength, Phys. Rev. Lett. 113 (2014) 1–5, doi:10.1103/PhysRevLett.113.106104.
[5] F.H. Cao, Y.J. Wang, L.H. Dai, Novel atomic-scale mechanism of incipient plasticity in a chemically complex CrCoNi medium-entropy alloy associated with inhomogeneity in local chemical environment, Acta Mater. 194 (2020) 283–294, doi:10.1016/j.actamat.2020.05.042.
[6] J.M. Rickman, H.M. Chan, M.P. Harmer, J.A. Smeltzer, C.J. Marvel, A. Roy, G. Balasubramanian, Materials informatics for the screening of multi-principal elements and high-entropy alloys, Nat. Commun. 10 (2019) 2618, doi:10.1038/s41467-019-10533-1.
[7] Y. Zhao, J.M. Park, D.H. Lee, E.J. Song, J.Y. Suh, U. Ramamurty, J. il Jang, Influences of hydrogen charging method on the hydrogen distribution and nanomechanical properties of face-centered cubic high-entropy alloy: a comparative study, Scr. Mater. 168 (2019) 76–80, doi:10.1016/j.scriptamat.2019.04.025.
[8] S. Gorsse, C. Hutchinson, M. Gouné, R. Banerjee, Additive manufacturing of metals: a brief review of the characteristic microstructures and properties of steels, Ti-6Al-4V and high-entropy alloys, Sci. Technol. Adv. Mater. 18 (2017) 584–610, doi:10.1080/14686996.2017.1361305.
[9] J.X. Chen, Y. Chen, J.P. Liu, T.W. Liu, L.H. Dai, Anomalous size effect in micron-scale CoCrNi medium-entropy alloy wire, Scr. Mater. 199 (2021) 113897, doi:10.1016/j.scriptamat.2021.113897.
[10] Y. Zhang, T.T. Zuo, Z. Tang, M.C. Gao, K.A. Dahmen, P.K. Liaw, Z.P. Lu, Microstructures and properties of high-entropy alloys, Prog. Mater. Sci. 61 (2014) 1–93, doi:10.1016/j.pmatsci.2013.10.001.
[11] Z. Li, S. Zhao, R.O. Ritchie, M.A. Meyers, Mechanical properties of high-entropy alloys with emphasis on face-centered cubic alloys, Prog. Mater. Sci. 102 (2019) 296–345, doi:10.1016/j.pmatsci.2018.12.003.
[12] E.P. George, D. Raabe, R.O. Ritchie, High-entropy alloys, Nat. Rev. Mater. 4 (2019) 515–534, doi:10.1038/s41578-019-0121-4.
[13] B. Cantor, I.T.H. Chang, P. Knight, A.J.B. Vincent, Microstructural development in equiatomic multicomponent alloys, Mater. Sci. Eng. A 375–377 (2004) 213–218, doi:10.1016/j.msea.2003.10.257.
[14] J. Yeh, S. Chen, S. Lin, J. Gan, T. Chin, T. Shun, C. Tsau, Nanostructured high-entropy alloys with multiple principal elements : novel alloy design concepts and outcomes, Adv. Eng. Mater. (2004) 299–303, doi:10.1002/adem.200300567.
[15] Z. Zhang, H. Sheng, Z. Wang, B. Gludovatz, Z. Zhang, E.P. George, Q. Yu, S.X. Mao, R.O. Ritchie, Dislocation mechanisms and 3D twin architectures generate exceptional strength-ductility-toughness combination in CrCoNi medium-entropy alloy, Nat. Commun. 8 (2017) 14390, doi:10.1038/ncomms14390.
[16] M. Naeem, H. He, F. Zhang, H. Huang, S. Harjo, T. Kawasaki, B. Wang, S. Lan, Z. Wu, F. Wang, Y. Wu, Z. Lu, Z. Zhang, C.T. Liu, X. Wang, Cooperative deformation in high-entropy alloys at ultralow temperatures, Sci. Adv. 6 (2020) eaax4002, doi:10.1126/sciadv.aax4002.
[17] E. Ma, Unusual dislocation behavior in high-entropy alloys, Scr. Mater. 181 (2020) 127–133, doi:10.1016/j.scriptamat.2020.02.021.
[18] P. Shi, R. Li, Y. Li, Y. Wen, Y. Zhong, W. Ren, Z. Shen, T. Zheng, J. Peng, X. Liang, P. Hu, N. Min, Y. Zhang, Y. Ren, P.K. Liaw, D. Raabe, Y.D. Wang, Hierarchical crack buffering triples ductility in eutectic herringbone high-entropy alloys, Science 373 (2021) 912–918, doi:10.1126/science.abf6986.
[19] Q. Pan, L. Zhang, R. Feng, Q. Lu, K. An, A.C. Chuang, J.D. Poplawsky, P.K. Liaw, L. Lu, Gradient cell–structured high-entropy alloy with exceptional strength and ductility, Science 374 (2021) 984–989, doi:10.1126/science.abj8114.
[20] Z. Lei, X. Liu, Y. Wu, H. Wang, S. Jiang, S. Wang, X. Hui, Y. Wu, B. Gault, P. Kontis, D. Raabe, L. Gu, Q. Zhang, H. Chen, H. Wang, J. Liu, K. An, Q. Zeng, T.G. Nieh, Z. Lu, Enhanced strength and ductility in a high-entropy alloy via ordered oxygen complexes, Nature 563 (2018) 546–550, doi:10.1038/s41586-018-0685-y.
[21] Y. Yang, T. Chen, L. Tan, J.D. Poplawsky, K. An, Y. Wang, G.D. Samolyuk, K. Littrell, A.R. Lupini, A. Borisevich, E.P. George, Bifunctional nanoprecipitates strengthen and ductilize a medium-entropy alloy, Nature 595 (2021) 245–249, doi:10.1038/s41586-021-03607-y.
[22] S. Wei, S.J. Kim, J.Y. Kang, Y. Zhang, Y. Zhang, T. Furuhara, E.S. Park, C.C. Tasan, Natural-mixing guided design of refractory high-entropy alloys with as-cast tensile ductility, Nat. Mater. 19 (2019) 1175–1181, doi:10.1038/s41563-020-0750-4.
[23] Y.J. Liang, L. Wang, Y. Wen, B. Cheng, Q. Wu, T. Cao, Q. Xiao, Y. Xue, G. Sha, Y. Wang, Y. Ren, X. Li, L. Wang, F. Wang, H. Cai, High-content ductile coherent nanoprecipitates achieve ultrastrong high-entropy alloys, Nat. Commun. 9 (2018) 4063, doi:10.1038/s41467-018-06600-8.
[24] B. Gludovatz, A. Hohenwarter, K.V.S. Thurston, H. Bei, Z. Wu, E.P. George, R.O. Ritchie, Exceptional damage-tolerance of a medium-entropy alloy CrCoNi at cryogenic temperatures, Nat. Commun. 7 (2016) 10602, doi:10.1038/ncomms10602.
[25] R. Feng, Y. Rao, C. Liu, X. Xie, D. Yu, Y. Chen, M. Ghazisaeidi, T. Ungar, H. Wang, K. An, P.K. Liaw, Enhancing fatigue life by ductile-transformable multicomponent B2 precipitates in a high-entropy alloy, Nat. Commun. 12 (2021) 3588, doi:10.1038/s41467-021-23689-6.
[26] X.H. Du, W.P. Li, H.T. Chang, T. Yang, G.S. Duan, B.L. Wu, J.C. Huang, F.R. Chen, C.T. Liu, W.S. Chuang, Y. Lu, M.L. Sui, E.W. Huang, Dual heterogeneous structures lead to ultrahigh strength and uniform ductility in a Co-Cr-Ni medium-entropy alloy, Nat. Commun. 11 (2020) 2390, doi:10.1038/s41467-020-16085-z.
[27] H. Luo, S.S. Sohn, W. Lu, L. Li, X. Li, C.K. Soundararajan, W. Krieger, Z. Li, D. Raabe, A strong and ductile medium-entropy alloy resists hydrogen embrittlement and corrosion, Nat. Commun. 11 (2020) 3081, doi:10.1038/s41467-020-16791-8.

[28] Q. Ding, Y. Zhang, X. Chen, X. Fu, D. Chen, S. Chen, L. Gu, F. Wei, H. Bei, Y. Gao, M. Wen, J. Li, Z. Zhang, T. Zhu, R.O. Ritchie, Q. Yu, Tuning element distribution, structure and properties by composition in high-entropy alloys, Nature 574 (2019) 223–227, doi:10.1038/s41586-019-1617-1.

[29] Z. Li, K.G. Pradeep, Y. Deng, D. Raabe, C.C. Tasan, Metastable high-entropy dual-phase alloys overcome the strength-ductility trade-off, Nature 534 (2016) 227–230, doi:10.1038/nature17981.

[30] B. Gludovatz, A. Hohenwarter, D. Catoor, E.H. Chang, E.P. George, R.O. Ritchie, A fracture-resistant high-entropy alloy for cryogenic applications, Science 345 (2014) 1153–1158, doi:10.1126/science.1254581.

[31] X.F. Liu, Z.L. Tian, X.F. Zhang, H.H. Chen, T.W. Liu, Y. Chen, Y.J. Wang, L.H. Dai, Self-sharpening" tungsten high-entropy alloy, Acta Mater. 186 (2020) 257–266, doi:10.1016/j.actamat.2020.01.005.

[32] Y. Lu, Y. Dong, H. Jiang, Z. Wang, Z. Cao, S. Guo, T. Wang, T. Li, P.K. Liaw, Promising properties and future trend of eutectic high entropy alloys, Scr. Mater. 187 (2020) 202–209, doi:10.1016/j.scriptamat.2020.06.022.

[33] Y. Lu, Y. Dong, S. Guo, L. Jiang, H. Kang, T. Wang, B. Wen, Z. Wang, J. Jie, Z. Cao, H. Ruan, T. Li, A promising new class of high-temperature alloys: eutectic high-entropy alloys, Sci. Rep. 4 (2014) 6200, doi:10.1038/srep06200.

[34] T. Bhattacharjee, R. Zheng, Y. Chong, S. Sheikh, S. Guo, I.T. Clark, T. Okawa, I.S. Wani, P.P. Bhattacharjee, A. Shibata, N. Tsuji, Effect of low temperature on tensile properties of $AlCoCrFeNi_{2.1}$ eutectic high entropy alloy, Mater. Chem. Phys. 210 (2018) 207–212, doi:10.1016/j.matchemphys.2017.06.023.

[35] T. Bhattacharjee, I.S. Wani, S. Sheikh, I.T. Clark, T. Okawa, S. Guo, P.P. Bhattacharjee, N. Tsuji, Simultaneous strength-ductility enhancement of a nano-lamellar $AlCoCrFeNi_{2.1}$ eutectic high entropy alloy by Cryo-rolling and annealing, Sci. Rep. 8 (2018) 3276, doi:10.1038/s41598-018-21385-y.

[36] S.R. Reddy, S. Yoshida, U. Sunkari, A. Lozinko, J. Joseph, R. Saha, D. Fabijanic, S. Guo, P.P. Bhattacharjee, N. Tsuji, Engineering heterogeneous microstructure by severe warm-rolling for enhancing strength-ductility synergy in eutectic high entropy alloys, Mater. Sci. Eng. A 764 (2019) 138226, doi:10.1016/j.msea.2019.138226.

[37] P. Shi, W. Ren, T. Zheng, Z. Ren, X. Hou, J. Peng, P. Hu, Y. Gao, Y. Zhong, P.K. Liaw, Enhanced strength–ductility synergy in ultrafine-grained eutectic high-entropy alloys by inheriting microstructural lamellae, Nat. Commun. 10 (2019) 489, doi:10.1038/s41467-019-08460-2.

[38] S.R. Reddy, S. Yoshida, T. Bhattacharjee, N. Sake, A. Lozinko, S. Guo, P.P. Bhattacharjee, N. Tsuji, Nanostructuring with structural-compositional dual heterogeneities enhances strength-ductility synergy in eutectic high entropy alloy, Sci. Rep. 9 (2019) 11505, doi:10.1038/s41598-019-47983-y.

[39] T. Xiong, S. Zheng, J. Pang, X. Ma, High-strength and high-ductility $AlCoCrFeNi_{2.1}$ eutectic high-entropy alloy achieved via precipitation strengthening in a heterogeneous structure, Scr. Mater. 186 (2020) 336–340, doi:10.1016/j.scriptamat.2020.04.035.

[40] Y. Zhu, S. Zhou, Z. Xiong, Y.J. Liang, Y. Xue, L. Wang, Enabling stronger eutectic high-entropy alloys with larger ductility by 3D printed directional lamellae, Addit. Manuf. 39 (2021) 101901, doi:10.1016/j.addma.2021.101901.

[41] J. Ren, Y. Zhang, D. Zhao, Y. Chen, S. Guan, Y. Liu, L. Liu, S. Peng, F. Kong, J.D. Poplawsky, G. Gao, T. Voisin, K. An, Y.M. Wang, K.Y. Xie, T. Zhu, W. Chen, Strong yet ductile nanolamellar high-entropy alloys by additive manufacturing, Nature 608 (2022) 62–68, doi:10.1038/s41586-022-04914-8.

[42] X. Wu, M. Yang, F. Yuan, G. Wu, Y. Wei, X. Huang, Y. Zhu, Heterogeneous lamella structure unites ultrafine-grain strength with coarse-grain ductility, Proc. Natl. Acad. Sci. USA 112 (2015) 14501–14505, doi:10.1073/pnas.1517193112.

[43] J.K. Hwang, I.C. Yi, I.H. Son, J.Y. Yoo, B. Kim, A. Zargaran, N.J. Kim, Microstructural evolution and deformation behavior of twinning-induced plasticity (TWIP) steel during wire drawing, Mater. Sci. Eng. A 644 (2015) 41–52, doi:10.1016/j.msea.2015.07.034.

[44] J.K. Hwang, Correlation of strain path, texture, twinning, and mechanical properties in twinning-induced plasticity steel during wire drawing, Materials 13 (2020) (Basel), doi:10.3390/ma13102250.

[45] I.S. Wani, T. Bhattacharjee, S. Sheikh, I.T. Clark, M.H. Park, T. Okawa, S. Guo, P.P. Bhattacharjee, N. Tsuji, Cold-rolling and recrystallization textures of a nano-lamellar $AlCoCrFeNi_{2.1}$ eutectic high entropy alloy, Intermetallics 84 (2017) 42–51, doi:10.1016/j.intermet.2016.12.018.

[46] X. Gao, Y. Lu, B. Zhang, N. Liang, G. Wu, G. Sha, J. Liu, Y. Zhao, Microstructural origins of high strength and high ductility in an $AlCoCrFeNi_{2.1}$ eutectic high-entropy alloy, Acta Mater. 141 (2017) 59–66, doi:10.1016/j.actamat.2017.07.041.

[47] Q. Wang, Y. Lu, Q. Yu, Z. Zhang, The exceptional strong face-centered cubic phase and semi-coherent phase boundary in a eutectic dual-phase high entropy alloy AlCoCrFeNi, Sci. Rep. 8 (2018) 14910, doi:10.1038/s41598-018-33330-0.

[48] I.S. Wani, T. Bhattacharjee, S. Sheikh, P.P. Bhattacharjee, S. Guo, N. Tsuji, Tailoring nanostructures and mechanical properties of $AlCoCrFeNi_{2.1}$ eutectic high entropy alloy using thermo-mechanical processing, Mater. Sci. Eng. A 675 (2016) 99–109, doi:10.1016/j.msea.2016.08.048.

[49] I.S. Wani, T. Bhattacharjee, S. Sheikh, Y.P. Lud, S. Chatterjee, P.P. Bhattacharjeea, S. Guo, N. Tsujib, Ultrafine-grained $AlCoCrFeNi_{2.1}$ eutectic high-entropy alloy, Mater. Res. Lett. 4 (2016) 174–179, doi:10.1080/21663831.2016.1160451.

[50] Y. Dong, X. Gao, Y. Lu, T. Wang, T. Li, A multi-component $AlCrFe2Ni_2$ alloy with excellent mechanical properties, Mater. Lett. 169 (2016) 62–64, doi:10.1016/j.matlet.2016.01.096.

[51] Q. Wu, Z. Wang, T. Zheng, D. Chen, Z. Yang, J. Li, J. jung Kai, J. Wang, A casting eutectic high entropy alloy with superior strength-ductility combination, Mater. Lett. 253 (2019) 268–271, doi:10.1016/j.matlet.2019.06.067.

[52] W. Zhang, L. Liu, S. Peng, J. Ren, F. Wu, J. Shang, M. Chen, Y. Zhang, Z. Zhao, J. Qi, B. Wang, W. Chen, The tensile property and notch sensitivity of $AlCoCrFeNi_{2.1}$ high entropy alloy with a novel "steel-frame" eutectic microstructure, J. Alloys Compd. 863 (2021) 158747, doi:10.1016/j.jallcom.2021.158747.

[53] L. Wang, C. Yao, J. Shen, Y. Zhang, T. Wang, Y. Ge, L. Gao, G. Zhang, Microstructures and room temperature tensile properties of as-cast and directionally solidified $AlCoCrFeNi_{2.1}$ eutectic high-entropy alloy, Intermetallics 118 (2020) 106681, doi:10.1016/j.intermet.2019.106681.

[54] S.R. Reddy, U. Sunkari, A. Lozinko, R. Saha, S. Guo, P.P. Bhattacharjee, Microstructural design by severe warm-rolling for tuning mechanical properties of $AlCoCrFeNi_{2.1}$ eutectic high entropy alloy, Intermetallics 114 (2019) 106601, doi:10.1016/j.intermet.2019.106601.

[55] P. Czarkowski, A.T. Krawczyńska, T. Brynk, M. Nowacki, M. Lewandowska, K.J. Kurzydłowski, Cryogenic strength and microstructure of a hydrostatically extruded austenitic steel 1.4429 (AISI 316LN), Cryogenics 64 (2014) 1–4 (Guildf), doi:10.1016/j.cryogenics.2014.07.014.

[56] K. Han, V.J. Toplosky, R. Walsh, C. Swenson, B. Lesch, V.I. Pantsyrnyi, Properties of high strength Cu-Nb conductor for pulsed magnet applications, IEEE Trans. Appl. Supercond. 12 (2002) 1176–1180, doi:10.1109/TASC.2002.1018611.

[57] D. Li, C. Li, T. Feng, Y. Zhang, G. Sha, J.J. Lewandowski, P.K. Liaw, Y. Zhang, High-entropy $Al_{0.3}CoCrFeNi$ alloy fibers with high tensile strength and ductility at ambient and cryogenic temperatures, Acta Mater. 123 (2017) 285–294, doi:10.1016/j.actamat.2016.10.038.

[58] J.P. Liu, J.X. Chen, T.W. Liu, C. Li, Y. Chen, L.H. Dai, Superior strength-ductility CoCrNi medium-entropy alloy wire, Scr. Mater. 181 (2020) 19–24, doi:10.1016/j.scriptamat.2020.02.002.

[59] Y.H. Jo, W.M. Choi, D.G. Kim, A. Zargaran, K. Lee, H. Sung, S.S. Sohn, H.S. Kim, B.J. Lee, S. Lee, Utilization of brittle σ phase for strengthening and strain hardening in ductile VCrFeNi high-entropy alloy, Mater. Sci. Eng. A 743 (2019) 665–674, doi:10.1016/j.msea.2018.11.136.

[60] B. Gan, J.M. Wheeler, Z. Bi, L. Liu, J. Zhang, H. Fu, Superb cryogenic strength of equiatomic CrCoNi derived from gradient hierarchical microstructure, J. Mater. Sci. Technol. 35 (2019) 957–961, doi:10.1016/j.jmst.2018.12.002.

[61] S. Wang, M. Wu, D. Shu, G. Zhu, D. Wang, B. Sun, Mechanical instability and tensile properties of TiZrHfNbTa high entropy alloy at cryogenic temperatures, Acta Mater. 201 (2020) 517–527, doi:10.1016/j.actamat.2020.10.044.

[62] J.M. Park, J. Moon, J.W. Bae, D.H. Kim, Y.H. Jo, S. Lee, H.S. Kim, Role of BCC phase on tensile behavior of dual-phase $Al_{0.5}CoCrFeMnNi$ high-entropy alloy at cryogenic temperature, Mater. Sci. Eng. A 746 (2019) 443–447, doi:10.1016/j.msea.2019.01.041.

[63] J. Yang, Y.H. Jo, D.W. Kim, W.M. Choi, H.S. Kim, B.J. Lee, S.S. Sohn, S. Lee, Effects of transformation-induced plasticity (TRIP) on tensile property improvement of Fe45Co30Cr10V10Ni5-xMnx high-entropy alloys, Mater. Sci. Eng. A 772 (2020) 138809, doi:10.1016/j.msea.2019.138809.

[64] P. Sathiyamoorthi, P. Asghari-Rad, J.M. Park, J. Moon, J.W. Bae, A. Zargaran, H.S. Kim, Exceptional cryogenic strength-ductility synergy in $Al_{0.3}CoCrNi$ medium-entropy alloy through heterogeneous grain structure and nano-scale precipitates, Mater. Sci. Eng. A 766 (2019) 138372, doi:10.1016/j.msea.2019.138372.

[65] K. Tang, Y.K. Wu, R. Wei, L.B. Chen, S. Lu, Y.L. Qi, F. Jiang, J. Sun, Achieving superior cryogenic tensile properties in a Ti-doped $(Fe_{40}Mn_{40}Co_{10}Cr_{10})96.7C3.3$ high-entropy alloy by recovering deformation twinning, Mater. Sci. Eng. A 808 (2021) 140927, doi:10.1016/j.msea.2021.140927.

[66] K. Górecki, P. Bała, W. Bednarczyk, J. Kawałko, Cryogenic behaviour of the $Al_5Ti_5Co_{35}Ni_{35}Fe_{20}$ multi-principal component alloy, Mater. Sci. Eng. A 745 (2019) 346–352, doi:10.1016/j.msea.2019.01.001.

[67] P. Czarkowski, A.T. Krawczynska, R. Slesinski, T. Brynk, J. Budniak, M. Lewandowska, K.J. Kurzydlowski, Low temperature mechanical properties of 316L type stainless steel after hydrostatic extrusion, Fusion Eng. Des. 86 (2011) 2517–2521, doi:10.1016/j.fusengdes.2010.12.067.

[68] C. Zheng, W. Yu, Effect of low-temperature on mechanical behavior for an AISI 304 austenitic stainless steel, Mater. Sci. Eng. A 710 (2018) 359–365, doi:10.1016/j.msea.2017.11.003.

[69] S.S. Sohn, S. Hong, J. Lee, B.C. Suh, S.K. Kim, B.J. Lee, N.J. Kim, S. Lee, Effects of Mn and Al contents on cryogenic-temperature tensile and Charpy impact properties in four austenitic high-Mn steels, Acta Mater. 100 (2015) 39–52, doi:10.1016/j.actamat.2015.08.027.

[70] H.S. Shin, H.M. Lee, M.S. Kim, Impact tensile behavior of 9% nickel steel at low temperature, Int. J. Impact Eng. 24 (2000) 571–581, doi:10.1016/S0734-743X(99)00181-5.

[71] M. Chen, J. He, J. Li, H. Liu, S. Xing, G. Wang, Excellent cryogenic strength-ductility synergy in duplex stainless steel with heterogeneous lamella structure, Mater. Sci. Eng. A 831 (2022) 142335, doi:10.1016/j.msea.2021.142335.

[72] C.K. Syn, S. Jin, J.W. Morris, Cryogenic fracture toughness of 9Ni Steel enhanced through grain refinement, Metall. Trans. A 7 (1976) 1827–1832, doi:10.1007/BF02654977.

[73] N. Koga, T. Nameki, O. Umezawa, V. Tschan, K.P. Weiss, Tensile properties and deformation behavior of ferrite and austenite duplex stainless steel at cryogenic temperatures, Mater. Sci. Eng. A 801 (2021) 140442, doi:10.1016/j.msea.2020.140442.

[74] D.F. Li, C.G. Fan, Y.Y. Li, H.M. Cheng, Tensile properties and deformation-induced martensitic transformation, Adv. Cryog. Eng. 42 (1996) 307–313, doi:10.1007/978-1-4757-9059-7_41.
[75] Y. Lu, X. Gao, L. Jiang, Z. Chen, T. Wang, J. Jie, H. Kang, Y. Zhang, S. Guo, H. Ruan, Y. Zhao, Z. Cao, T. Li, Directly cast bulk eutectic and near-eutectic high entropy alloys with balanced strength and ductility in a wide temperature range, Acta Mater. 124 (2017) 143–150, doi:10.1016/j.actamat.2016.11.016.
[76] G. Laplanche, A. Kostka, O.M. Horst, G. Eggeler, E.P. George, Microstructure evolution and critical stress for twinning in the CrMnFeCoNi high-entropy alloy, Acta Mater. 118 (2016) 152–163, doi:10.1016/j.actamat.2016.07.038.
[77] R.K. Nutor, Q. Cao, R. Wei, Q. Su, G. Du, X. Wang, F. Li, D. Zhang, J. Jiang, A dual-phase alloy with ultrahigh strength-ductility synergy over a wide temperature range, Sci. Adv. 5 (2021) eabi4404, doi:10.1126/sciadv.abi4404.
[78] J. Moon, J.M. Park, J.W. Bae, N. Kang, J. Oh, H. Shin, H.S. Kim, Hetero-deformation-induced strengthening by twin-mediated martensitic transformation in an immiscible medium-entropy alloy, Scr. Mater. 186 (2020) 24–28, doi:10.1016/j.scriptamat.2020.04.044.
[79] P. Sathiyamoorthi, J. Moon, J.W. Bae, P. Asghari-Rad, H.S. Kim, Superior cryogenic tensile properties of ultrafine-grained CoCrNi medium-entropy alloy produced by high-pressure torsion and annealing, Scr. Mater. 163 (2019) 152–156, doi:10.1016/j.scriptamat.2019.01.016.
[80] W. Li, T.H. Chou, T. Yang, W.S. Chuang, J.C. Huang, J. Luan, X. Zhang, X. Huo, H. Kong, Q. He, X. Du, C.T. Liu, F.R. Chen, Design of ultrastrong but ductile medium-entropy alloy with controlled precipitations and heterogeneous grain structures, Appl. Mater. Today 23 (2021) 101037, doi:10.1016/j.apmt.2021.101037.
[81] S.J. Sun, Y.Z. Tian, H.R. Lin, H.J. Yang, X.G. Dong, Y.H. Wang, Z.F. Zhang, Achieving high ductility in the 1.7 GPa grade CoCrFeMnNi high-entropy alloy at 77 K, Mater. Sci. Eng. A 740–741 (2019) 336–341, doi:10.1016/j.msea.2018.10.094.
[82] D.G. Kim, Y.H. Jo, J. Yang, W.M. Choi, H.S. Kim, B.J. Lee, S.S. Sohn, S. Lee, Ultrastrong duplex high-entropy alloy with 2 GPa cryogenic strength enabled by an accelerated martensitic transformation, Scr. Mater. 171 (2019) 67–72, doi:10.1016/j.scriptamat.2019.06.026.
[83] J.B. Seol, J.W. Bae, J.G. Kim, H. Sung, Z. Li, H.H. Lee, S.H. Shim, J.H. Jang, W.S. Ko, S.I. Hong, H.S. Kim, Short-range order strengthening in boron-doped high-entropy alloys for cryogenic applications, Acta Mater. 194 (2020) 366–377, doi:10.1016/j.actamat.2020.04.052.
[84] D. Caillard, B. Bienvenu, E. Clouet, Anomalous slip in body-centred cubic metals, Nature 609 (2022) 936–941, doi:10.1016/S0921-5093(01)00958-3.
[85] M.H. Loretto, R.J. Wasilewski, Slip systems in NiAl single crystals at 300°k and 77 °K, Philos. Mag. 23 (1971) 1311–1328, doi:10.1080/14786437108217004.
[86] J. Li, Y. Chen, Q. He, X. Xu, H. Wang, C. Jiang, B. Liu, Q. Fang, Y. Liu, Y. Yang, P.K. Liaw, C.T. Liu, Heterogeneous lattice strain strengthening in severely distorted crystalline solids, Proc. Natl. Acad. Sci. USA 119 (2022) e2200607119, doi:10.1073/pnas.2200607119.
[87] I. Salehinia, D.F. Bahr, Crystal orientation effect on dislocation nucleation and multiplication in FCC single crystal under uniaxial loading, Int. J. Plast. 52 (2014) 133–146, doi:10.1016/j.ijplas.2013.04.010.
[88] S. Dodla, P. Thiem, M. Krüger, D. Dietrich, A. Bertram, Microstructure, flow behavior, and bulk texture evolution of cold drawn copper-silver composites, J. Alloys Compd. 647 (2015) 519–527, doi:10.1016/j.jallcom.2015.06.145.
[89] E.O. Hall, The deformation and ageing of mild steel: II characteristics of the Lüders deformation, Proc. Phys. Soc. Sect. B 64 (1951) 742–747, doi:10.1088/0370-1301/64/9/302.
[90] Y. Ateba Betanda, A.L. Helbert, F. Brisset, M.H. Mathon, T. Waeckerlé, T. Baudin, Measurement of stored energy in Fe-48%Ni alloys strongly cold-rolled using three approaches: neutron diffraction, dillamore and KAM approaches, Mater. Sci. Eng. A 614 (2014) 193–198, doi:10.1016/j.msea.2014.07.037.
[91] N.A. Fleck, G.M. Muller, M.F. Ashby, J.W. Hutchinson, Strain gradient plasticity: theory and experiment, Acta Metall. Mater. 42 (1994) 475–487, doi:10.1016/0956-7151(94)90502-9.
[92] H. Gao, Y. Huang, Geometrically necessary dislocation and size-dependent plasticity, Scr. Mater. 48 (2003) 113–118, doi:10.1016/S1359-6462(02)00329-9.
[93] Q. Liu, D. Juul Jensen, N. Hansen, Effect of grain orientation on deformation structure in cold-rolled polycrystalline aluminium, Acta Mater. 46 (1998) 5819–5838, doi:10.1016/S1359-6454(98)00229-8.
[94] H.L. Cox, The elasticity and strength of paper and other fibrous materials, Br. J. Appl. Phys. 72 (1952) 72–79, doi:10.1088/0508-3443/3/3/302.
[95] H.G. Kim, Effects of fiber aspect ratio evaluated by elastic analysis in discontinuous composites, J. Mech. Sci. Technol. 22 (2008) 411–419, doi:10.1007/s12206-007-1208-1.
[96] L.H. Dai, Z. Ling, Y.L. Bai, Strain gradient-strengthening law for particle reinforced metal matrix composites, Scr. Mater. 41 (1999) 245–251, doi:10.1016/S1359-6462(99)00153-0.
[97] N.A. Fleck, J.W. Hutchinson, Strain gradient plasticity, Adv. Appl. Mech. 33 (1997) 295–361, doi:10.1016/S0065-2156(08)70388-0.
[98] W.D. Nix, H. Gao, Indentation size effects in crystalline materials: a law for strain gradient plasticity, J. Mech. Phys. Solids 46 (1998) 411–425, doi:10.1016/S0022-5096(97)00086-0.
[99] S.I. Hong, C. Laird, Mechanisms of slip mode modification in F.C.C. solid solutions, Acta Metall. Mater. 38 (1990) 1581–1594, doi:10.1016/0956-7151(90)90126-2.
[100] Q. Ding, X. Fu, D. Chen, H. Bei, B. Gludovatz, J. Li, Z. Zhang, E.P. George, Q. Yu, T. Zhu, R.O. Ritchie, Real-time nanoscale observation of deformation mechanisms in CrCoNi-based medium- to high-entropy alloys at cryogenic temperatures, Mater. Today 25 (2019) 21–27, doi:10.1016/j.mattod.2019.03.001.
[101] F. Otto, A. Dlouhý, C. Somsen, H. Bei, G. Eggeler, E.P. George, The influences of temperature and microstructure on the tensile properties of a CoCrFeMnNi high-entropy alloy, Acta Mater. 61 (2013) 5743–5755, doi:10.1016/j.actamat.2013.06.018.
[102] Z.C. Cordero, B.E. Knight, C.A. Schuh, Six decades of the Hall–Petch effect – a survey of grain-size strengthening studies on pure metals, Int. Mater. Rev. 61 (2016) 495–512, doi:10.1080/09506608.2016.1191808.
[103] I.J. Beyerlein, X. Zhang, A. Misra, Growth twins and deformation twins in metals, Annu. Rev. Mater. Res. 44 (2014) 329–363, doi:10.1146/annurev-matsci-070813-113304.
[104] Z. Pu, Z.C. Xie, R. Sarmah, Y. Chen, C. Lu, G. Ananthakrishna, L.H. Dai, Spatio-temporal dynamics of jerky flow in high-entropy alloy at extremely low temperature, Philos. Mag. 101 (2021) 154–178, doi:10.1080/14786435.2020.1822557.